A study on the ambient noise field at a hydroacoustic array near Robinson Crusoe Island

Sambell, K. A.M.; Smets, P. S.M.; Simons, D. G.; Snellen, M.; Evers, L. G.

Citation (APA)
Sambell, K. A. M., Smets, P. S. M., Simons, D. G., Snellen, M., & Evers, L. G. (2019). A study on the ambient noise field at a hydroacoustic array near Robinson Crusoe Island. *Geophysical Journal International*, *218*(1), 88-99. https://doi.org/10.1093/gji/ggz124

Important note
To cite this publication, please use the final published version (if applicable).
Please check the document version above.

A study on the ambient noise field at a hydroacoustic array near Robinson Crusoe Island

K.A.M. Sambell,[1,2,3] P.S.M. Smets [1,3] D.G. Simons,[2] M. Snellen[2] and L.G. Evers [1,3]

[1]*Department of Geoscience and Engineering, Faculty of Civil Engineering and Geosciences, Delft University of Technology, Stevinweg* 1, 2628 *CN Delft, The Netherlands. E-mail:* p.s.m.smets@tudelft.nl
[2]*Department of Operations and Control, Faculty of Aerospace Engineering, Delft University of Technology, Kluyverweg* 1, 2629 *HS Delft, The Netherlands*
[3]*R&D Seismology and Acoustics, Royal Netherlands Meteorological Institute (KNMI), P.O. Box* 201, 3730 *AE De Bilt, The Netherlands*

SUMMARY

Continuous long-term sound sources are recorded at hydroacoustic station H03S, a three-element hydrophone array south of Robinson Crusoe Island between 2014 April 23 and 2017 August 20. The origin of the signal between 3 and 20 Hz is investigated by using cross-correlation, array processing using plane wave beamforming and spectral analysis. One-bit normalization is successfully applied as a cross-correlation pre-processing step in order to suppress undesired earthquake events in the data. Traveltimes retrieved from averaged cross-correlations do not yield a coherent array direction of arrival. Averaged envelopes of the cross-correlations, however, indicate a coherent signal approaching H03S from a south–southwest direction. Beamforming indicates two dominant backazimuth directions: 172°–224° (Antarctica) and 242° (Monowai Volcanic Seamount). This continuous source field creates possibilities to investigate the applicability of acoustic thermometry at hydrophones H03 S1–S2. Cross-correlation and array processing indicate significant directional variation in local propagation, most likely related to the steep slope in the bathymetry near H03S. In addition, it is demonstrated that the ambient noise field is not sufficiently equipartitioned. It is shown that this causes a large error in the estimated temperature, primarily due to the short receiver spacing. These large errors have not been addressed in previous studies on deep-ocean acoustic thermometry. Hence, it is shown that acoustic thermometry does not perform well on small arrays such as H03S. The power spectral density yields a strong broadband signal in January–March, most likely related to iceberg noise. A narrow banded signal around 17 Hz between April and September corresponds to whale calls. The best-beam sound pressure levels towards Antarctica are compared to ERA5 climatologies for sea ice cover and normalized stress into the ocean, supporting the hypothesis of iceberg noise.

Key words: Time-series analysis; Spatial analysis; Persistence, memory, correlations, clustering; Interferrometry; Pacific Ocean; Antarctica.

1 INTRODUCTION

The International Monitoring System (IMS) is being established as a verification measure for the Comprehensive Nuclear-Test-Ban Treaty (CTBT). The IMS consists of a global network of seismometers, hydrophones and microbarometers that constantly monitor the underground, oceans and atmosphere for potential nuclear test explosions. In addition, the IMS measures noble gases and radionuclides to confirm the occurrence of a nuclear test.

The hydroacoustic monitoring network consists of 11 stations located in the main oceans around the world: five seismic T-phase stations on land and six underwater hydrophone stations. The five land-based seismometers positioned upon steep-sloped islands measure the hydroacoustic-to-seismic coupled energy (T-phase). All six hydrophone stations are located in the SOFAR (SOund Fixing And Ranging) channel, a low-velocity layer in the ocean that functions as an acoustical waveguide. Sound waves refract around the channel axis that enables them to travel for thousands of kilometres (e.g. Jensen *et al.* 2011). The SOFAR channel is characterized by a lower cutoff frequency of 3 Hz. The hydrophones have a flat amplitude response within 1–100 Hz and sample at 250 Hz (Dahlman *et al.* 2009).

The IMS hydroacoustic network has been used for various other monitoring applications studying earthquakes (de Groot-Hedlin

2005; Evers & Snellen 2015), underwater volcanoes (Watts *et al.* 2012; Green *et al.* 2013; Metz *et al.* 2016), marine mammals (Prior *et al.* 2012) and icebergs (Talandier *et al.* 2006; Evers *et al.* 2013; Matsumoto *et al.* 2014). The aforementioned sources confine the dominant sources of the hydroacoustic network's ambient noise field. Recent studies have shown the potential of passive hydroacoustic thermometry in the SOFAR channel using traveltime variations of ridge earthquakes (Evers & Snellen 2015) and by cross-correlating ambient signals recorded at two distinct IMS arrays, H10N and H10S, located near Ascension Island in the South Atlantic Ocean (Woolfe *et al.* 2015; Evers *et al.* 2017).

This study assesses the possibility for acoustic thermometry at IMS station H03 by cross-correlations, located near Robinson Crusoe Island, Chile, in the South Pacific Ocean (see Fig. 1). H03 is composed of two arrays, H03N and H03S, located north and south of the island separated by approximately 50 km. Both arrays consist of three hydrophones (H03N1–N3 and H03S1–S3) with an intersensor distance of 2 km (Dahlman *et al.* 2009). Previous studies by Woolfe *et al.* (2015) and Evers *et al.* (2017) applied cross-correlation (CC) algorithms to interarray receiver pairs, between array elements of the north and south arrays at Ascension Island (H10) and Wake Island (H11), yielding an intersensor distance of more than 100 km. Furthermore, Evers *et al.* (2017) applied cross-beam correlation techniques, cross-correlating the array beams retrieved by array processing. Interarray cross-correlation at H03 is not possible due to blocking by Robinson Crusoe Island. Hence, cross-correlation algorithms can only be applied to intra-array element pairs leading to 2 km receiver pairs. Implications of applying cross-correlation to close receiver pairs and the implication on acoustic thermometry are of interest in this study.

In this study, continuous ambient noise recordings at H03S from 2014 April to 2017 August are analysed. No earlier data are available since H03 was destroyed in 2010 by a tsunami and reinstalled in 2014 (Haralabus *et al.* 2014). The mean depth of the southern array is 827.6 m below mean sea level +4.2 m, −11.7 m and +7.3 m, for S1, S2 and S3, respectively. Deviations from the horizontal plane yield a slight tilt of the array normal vector, oriented down, with a declination of 0.6° towards −8.4° clockwise from north. H03S provides a clear path towards iceberg sound from the Antarctic Circumpolar Current, an important source of hydroacoustic ambient noise in the southern hemisphere. Iceberg sound originates from two different mechanisms: (1) iceberg break-up and disintegration processes create short-duration broadband pulses (1–440 Hz; Dziak *et al.* 2013), and (2) acoustic tremor of ice masses, possibly caused by fluid resonances within the ice masses, generate longer signals (Talandier *et al.* 2002; Chapp *et al.* 2005).

Variations of the ambient noise field can significantly affect the pair-wise cross-correlation results. Therefore, the ambient noise field observed at H03S is also characterized by array processing and spectral analysis in order to better understand the observed sources and their seasonal variation. Observations are combined with the ERA5 reanalysis data set of the Copernicus Climate Change Service (C3S; Hersbach & Dick 2016). ERA5 provides hourly estimates of various climate variables by combining observations with advanced modelling and data assimilation systems. In this study, monthly averaged daily mean estimates of atmospheric and oceanic climate variables are used.

The article is organized as follows. A brief overview of the applied methods is listed in Section 2. The corresponding cross-correlation and array processing results are stated in Section 3. The concept of thermometry applied to a single IMS station is given in Section 4. Spectral characterization of the ambient noise field is given

in Section 5. The obtained spectrograms are compared with Knudsen spectral empirical noise levels and seasonal variations in sea ice. Discussions and conclusions are stated in Sections 6 and 7.

2 METHODOLOGY

2.1 Cross-correlations and first-order thermometry

In a fully equipartitioned wavefield, the Green's function between a pair of receivers can be obtained through simple cross-correlations (Wapenaar *et al.* 2005). In application to recordings of ambient noise, this implies that the response to an impulsive source at one receiver is recorded at another receiver: a so-called virtual source is created (Shapiro & Campillo 2004; Bakulin & Calvert 2006). Applied to hydroacoustics, this allows the retrieval of the traveltime between that pair of receivers (Roux & Kuperman 2004). In general, equipartitioning implies isotropy (Snieder *et al.* 2007). For an anisotropic wavefield, however, it suffices to have sources located in the so-called Fresnel zones, areas near the line of sight between the two receivers (Snieder 2004). In that case, the retrieved Green's function will closely approximate the true Green's function (e.g. Wapenaar *et al.* 2010). In this study, for example, iceberg noise from the Antarctic Circumpolar observed at H03S will only yield the single-sided Green's function without its time reversed.

A commonly applied technique to retrieve the diffuse wavefield from cross-correlations is averaging, or in seismology jargon 'stacking', cross-correlation windows, if the wavefield is sufficiently isotropic (Boschi & Weemstra 2015). Accordingly, the phase velocity between the receiver pair is retrieved from the time-averaged cross-correlations, corresponding to the lag time at the maximum cross-correlation. The maximum cross-correlation is obtained from the envelope function applied to the averaged cross-correlations (Boschi *et al.* 2013). Incoherency between the cross-correlations due to anisotropy, however, precludes retrieval of the diffuse wavefield and thus the phase velocity and the corresponding traveltime. Alternatively, the cross-correlations can be averaged incoherently by averaging the envelope functions of each cross-correlation window, the so-called averaged envelopes, averaging only the outlining amplitudes or energy. As a consequence, removing the phase information from the cross-correlations by applying an envelope function does no longer provide the Green's function nor the true phase velocity (Bensen *et al.* 2007). Nevertheless, cross-correlations envelopes can approximate the phase velocity of the diffuse wavefield.

The speed of sound (*c*) in the ocean according to Medwin & Clay (1997) is,

$$c = 1449.2 + 4.6T - 0.055T^2 + 0.00029T^3$$
$$+ (1.34 - 0.01T)(S - 35) + 0.016z, \tag{1}$$

with depth (*z*), temperature (*T*) and salinity (*S*). Variations in temperature have the largest influence (Dushaw *et al.* 2009). Hence, a first-order approximation of eq. (1) can be assumed, and the expression for temperature as a function of sound speed and depth becomes,

$$T = \frac{c - 1449.2 - 0.016z}{4.6}, \tag{2}$$

ignoring higher order terms of *T* and assuming a constant salinity *S* = 35. Eq. (2) is used to estimate the ambient temperature between the receiver pair based on the approximated single-sided Green's function assuming a uniform medium.

In the remainder of this study, cross-correlations are performed using time windows of 1 hr with an overlap of 50 per cent. The data
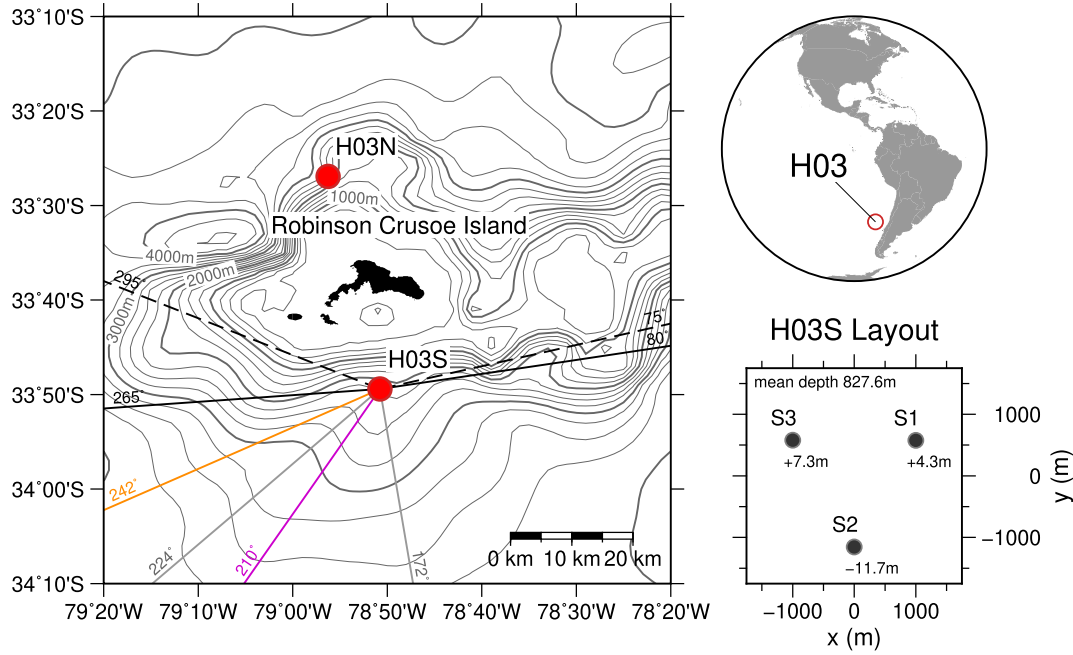
Figure 1. Map of the location of the hydroacoustic station H03 at Robinson Crusoe Island, Chile, in the South Pacific Ocean. The contour lines indicate the local bathymetry (depth below mean sea surface, in metre). The indicated backazimuth angles for H03S, clockwise from north, are referred to throughout the article.

are first filtered by a second-order bandpass filter between 3 and 5 Hz and then decimated by a factor 5 to a sampling frequency of 50 Hz. The bandwidth is chosen because the frequencies are high enough to ensure SOFAR channel propagation, while being low enough to high coherency between receivers. Then, one-bit normalization is applied (see Subsection 2.2).

2.2 One-bit pre-processing of the cross-correlation data

In order to cross-correlate the ambient noise field, undesired events such as earthquakes or instrumental irregularities in the data need to be suppressed. In this study, this is done by applying one-bit normalization as a pre-processing step as described by Bensen *et al.* (2007). The actual pressure recording of each sample point is replaced by either −1 or 1, depending on the sign of the recording. This results in a data stream with unit amplitude in which events and noise become equally important. It has been decided to use this method due to its computational efficiency and its ability to improve the cross-correlations obtained during this study.

Fig. 2 shows the normalized cross-correlations for S1–S2 on 2015 September 16 and 17, (i) without pre-processing and (ii) with one-bit normalization. The cross-correlation is performed using time windows of 2 hr with an overlap of 90 per cent. Fig. 2(a) shows a clear peak in the cross-correlation result at a lag time of 0.80 s. This value is determined by applying an envelope function to the averaged sum over all time windows. High cross-correlation coefficients at 0.80 s are related to the earthquake (22:46 UTC) and its aftershocks, all transient signals. The same peak is visible in Fig. 2(b), where one-bit normalization has been applied before cross-correlating. The maximum cross-correlation coefficient, however, appears at a lag time of −1.29 s corresponding to the ambient signals or noise field. Without one-bit normalization, the ambient noise field is completely dominated by the transient signals.

2.3 Array processing by plane wave beamforming

Beamforming operates on the entire array, in contrast to pair-wise cross-correlation. Beamforming is a signal summation process of delayed recordings, altering the array's interference pattern and so operating as a spatial filter. This yields an average array signal or beam with a signal-to-noise ratio (SNR) increase of $\sqrt{N}$, where N equals the number of array elements, under the assumption of uncorrelated noise. The array beam is characterized by a specific horizontal slowness vector ($\vec{p}$) assuming a propagating plane wave across a planar array. Signal coherency within a finite time-window is determined by the time-domain Fisher detector (Melton & Bailey 1957). For each time window, a discrete slowness grid is evaluated for the maximum Fisher ratio $F = N \cdot \text{SNR}^2 + 1$ yielding the best-beam and corresponding slowness vector of the most coherent signal within that window. Recordings are delayed by

$$t_i = -\vec{p} \cdot \vec{r}_i \tag{3}$$

with $\vec{r}_i$ the horizontal position of the receiver. The horizontal slowness is defined as,

$$\vec{p} = -c_{\text{app}}^{-1} \begin{pmatrix} \sin\phi \\ \cos\phi \end{pmatrix}, \tag{4}$$

with backazimuth angle ϕ clockwise relative to the north and the horizontal velocity across the array $c_{\text{app}} = \|\vec{p}\|^{-1}$, the so-called apparent velocity. Planar array beamforming cannot resolve the true phase velocity (c) of the incoming plane wave, which is related to the apparent velocity by

$$c_{\text{app}} = \frac{c}{\cos\theta}, \tag{5}$$

with θ the incidence angle of the plane wave from the horizontal. Variation in apparent velocity corresponds to different propagation modes of acoustic waves travelling towards H03S. Signals propagating in the SOFAR channel meander around the channel's axis, varying the incidence angle of the wavefield.
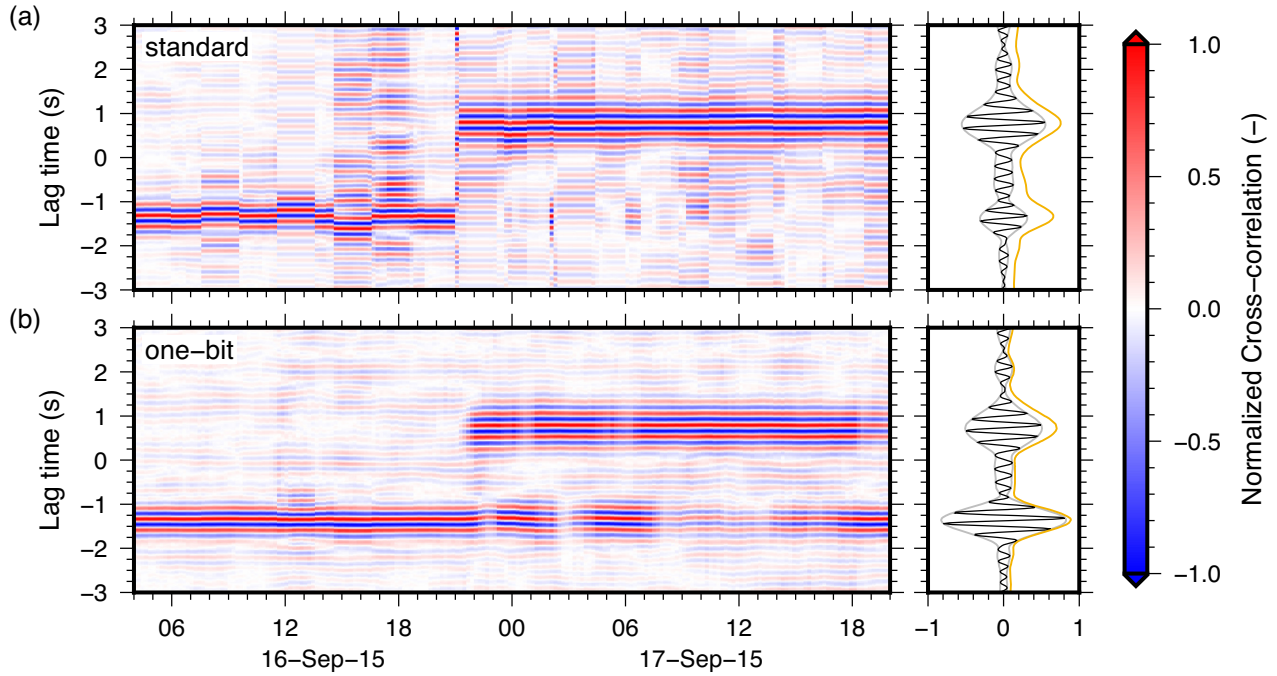
Figure 2. Normalized cross-correlation results for S1–S2 (a) without and (b) with one-bit normalization. Left-hand panel: two hourly cross-correlation results normalized per window. Right-hand panel: averaged cross-correlations (black) with their envelopes (grey) and averaged envelopes of the cross-correlations (orange). An earthquake with magnitude M_w 8.4 occurred on 2015 September 16 22:54:33 UTC west of Illapel, Chile (USGS).

Throughout this study, array processing is applied as follows: First, the data are bandpass filtered between 3 and 20 Hz using a second-order Butterworth filter. No decimation is applied, in contrast to the cross-correlations, to allow sufficient temporal resolution for time-delaying. Then, beamforming is applied to a sliding time window of 4096 samples (16.4 s) with an overlap of 50 per cent. The discrete slowness grid is defined from 0 to 360° for backazimuth and from 1450 to 1540 m s^{-1} for apparent velocity with steps of 1° and 2 m s^{-1}, respectively.

3 RESULTS

3.1 Cross-correlation

Fig. 3 shows the hourly cross-correlations between 2014 April 23 and 2017 August 20 for all three receiver pairs with the averaged cross-correlations shown on the right of each sub-figure. A negative lag time indicates that the signal is travelling in the opposite direction. Receiver pair orientations and retrieved traveltimes with corresponding backazimuth angles are listed in Table 1.

The cross-correlations between S1 and S2 (Fig. 3a) manifest a constant signal throughout the whole time-series. The averaged cross-correlations and averaged envelopes both indicate a consistent lag time. Vertical bands in the cross-correlation results, for example, see April–June in Fig. 3, most likely correspond to insufficiently suppressed transient earthquake events by the one-bit normalization. Both S2–S3 and S3–S1 indicate an increased source variability yielding lower averaged cross-correlation amplitudes with a stronger peak of the averaged envelopes at different lag times. From Figs 3(b) and (c), it is suggested that there is something common to signals at S3 that is not yet fully understood, but that results in cross-correlations that indicate arrivals (directions) varying with time. Combining the traveltimes retrieved from the averaged

cross-correlations does not yield a unique direction. The averaged envelopes, however, indicate a signal approaching H03S from the south–southwest in the direction of Antarctica.

The retrieved lag time for S1–S2 will be used for acoustic thermometry in Section 4.

3.2 Array processing

Fig. 4 shows the backazimuth for data measured at H03S between 2014 April 23 and 2017 August 20 for SNR $\geq$ 0.9. Directions of interest in Fig. 4 are also indicated in Fig. 1. Nearly no signals are detected outside the backazimuth range of 80° to 265°, most likely due to bathymetric blocking by Robinson Crusoe Island and its topographic spur, extending with depth (solid black line in Fig. 1). Contrarily, bathymetric blocking is expected in the range of 295° to 75° (dashed black line in Fig. 1), assuming a non-obstructed line-of-sight with a minimal depth of 500 m (approximately one acoustical wavelength at 3 Hz).

The backazimuth probability distribution (Fig. 4a) and backazimuth variation through time (Fig. 4b) indicate two dominant backazimuth directions which are back projected on the globe in Fig. 5:

(i) A swath from 172° to 224° (marked grey in Fig. 4) colour coded by its bathymetry in Fig. 5. The latter indicates sufficient depth to allow long distance SOFAR channel propagation towards H03S. The swath, pointing towards the Antarctic coast and the Antarctic Circumpolar Current, corresponds to the contour lines of the ERA5 sea ice cover within line-of-sight. This suggests observations of calving and breaking of icebergs near Antarctica, similar as shown by Matsumoto *et al.* (2014) for H03N during 2002–2008.

(ii) An intermittent, but frequent, signal from 242° (orange line) in the direction of the Kermadec volcanic arc, northeast of New
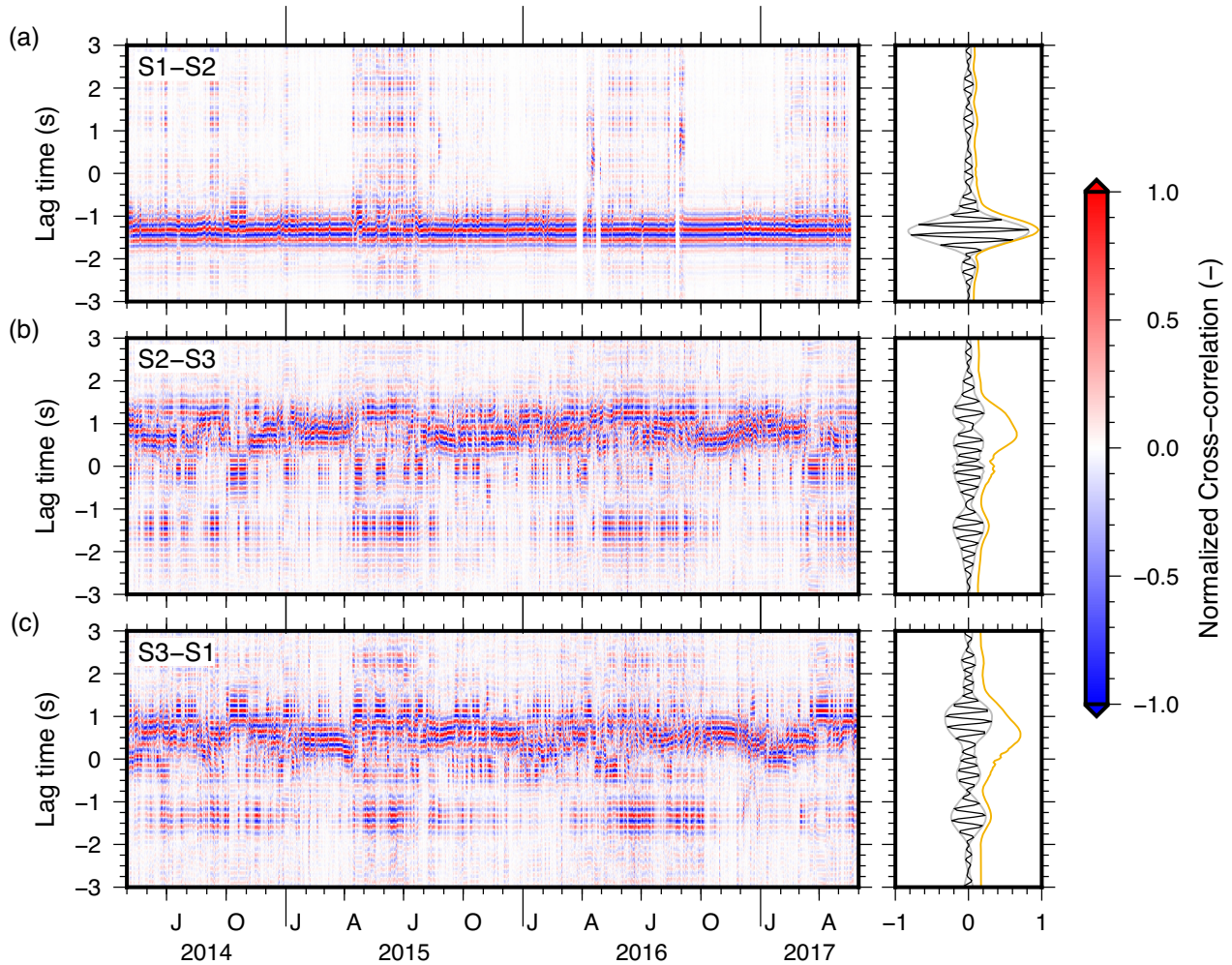
Figure 3. Cross-correlation results for the three different pairs: (a) S1–S2, (b) S2–S3 and (c) S3–S1. Left-hand panel: hourly cross-correlation results normalized per window. Right-hand panel: averaged cross-correlations (black) with their envelopes (grey) and averaged envelopes of the cross-correlations (orange).

Table 1. Retrieved traveltimes of the averaged cross-correlations and averaged cross-correlations envelopes shown in Fig. 3 and corresponding back-azimuth angles clockwise from north assuming a horizontal plane wave propagation with a constant velocity of 1481.7 m s^{-1} (see Section 4). A backazimuth angle range is given since any signal arriving at a receiver pair off the receiver pair axis has an intrinsic ambiguity.

Pair	Averaged CC		Averaged CC envelopes	
	Lag	ϕ	Lag	ϕ
S1–S2	−1.32 s	210±10°	−1.32 s	210±10°
S2–S3	0.00 s	150±90°	0.75 s	150±56°
S3–S1	0.96 s	270±45°	0.56 s	270±65°

Zealand. This signal most likely corresponds to the Monowai volcanic seamount, the most active underwater volcano of the region. Monowai is located halfway between Tonga and the Kermadec Islands, with a true geodesic angle of arrival of 243.9° at approximately 9153 km distance (Watts *et al.* 2012; Metz *et al.* 2016). Most signals with an SNR of 0.9 and more correspond to a backazimuth direction of 242° and 243°, with probabilities of 68.0 and 5.6 per cent, respectively.

The purple line at 210° in Fig. 4 corresponds to the azimuth angle of S1–S2 clockwise from north. Part of the received signal lies in the

Fresnel zone of S1–S2, supporting the concept of applying acoustic thermometry as introduced in Subsection 2.1 and demonstrated in Section 4.

4 THE CONCEPT OF THERMOMETRY APPLIED TO A SINGLE IMS STATION

The temperature is estimated from the retrieved traveltime of the cross-correlations assuming a homogeneous medium and maximal lag time propagation (along the receiver pair axis). The latter is supported by the beamforming results, indicating ambient detections within the southern Fresnel zone of S1–S2.

Fig. 6 shows the lag time histogram for S1–S2 retrieved from both cross-correlations (CC) and plane wave beamforming. The cross-correlations lag time corresponds to the maximum value of the cross-correlation envelope for each individual time window. Cross-correlations are first averaged using a sliding 30-d window. Fig. 6(a) yields a maximum CC lag time of −1.324 ±0.011 s, only including time bins with maximum cross-correlation values within −1.26 s and −1.36 s and assuming a normal distribution with the two standard deviation limit stated as the uncertainty. The time range is chosen such that artefacts such as cycle-skipping and sources outside the southern Fresnel zone are excluded.
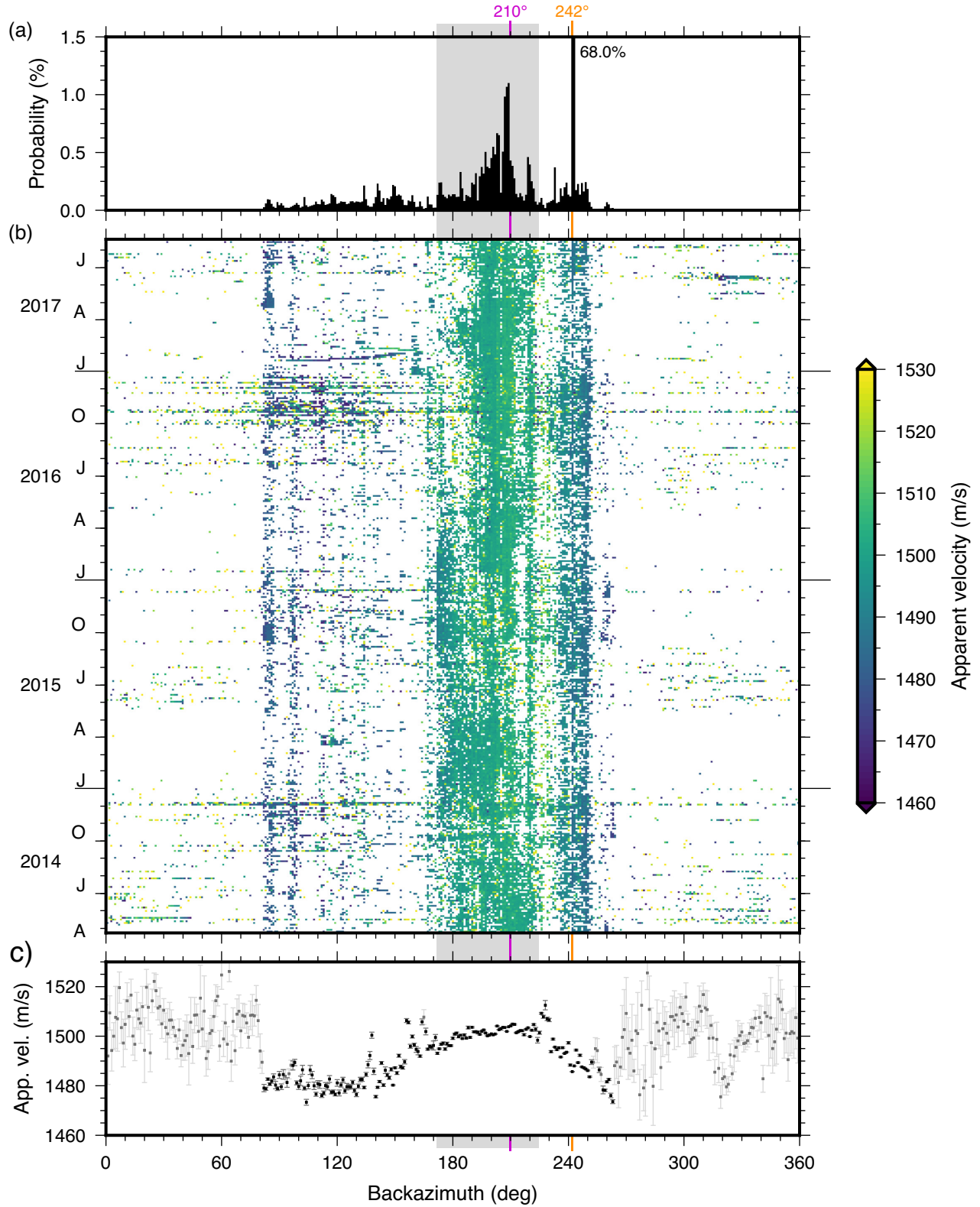
Figure 4. Beamforming results for detections at H03S with SNR ≥ 0.9. (a) Probability distribution per backazimuth with two main areas: 172°–224° (grey) and 242° (orange). The purple line at 210° corresponds with the bearing angle between S1 and S2. (b) Backazimuth through time averaged per three days colour coded by apparent velocity. (c) Average apparent velocity per backazimuth with 95 per cent confidence interval. Light grey indicates confidences interval above 2 m s^{-1}.

As a comparison, the lag time is estimated from the array processing results. Plane wave time difference between S1 and S2 are obtained from beamforming by applying eq. (3)

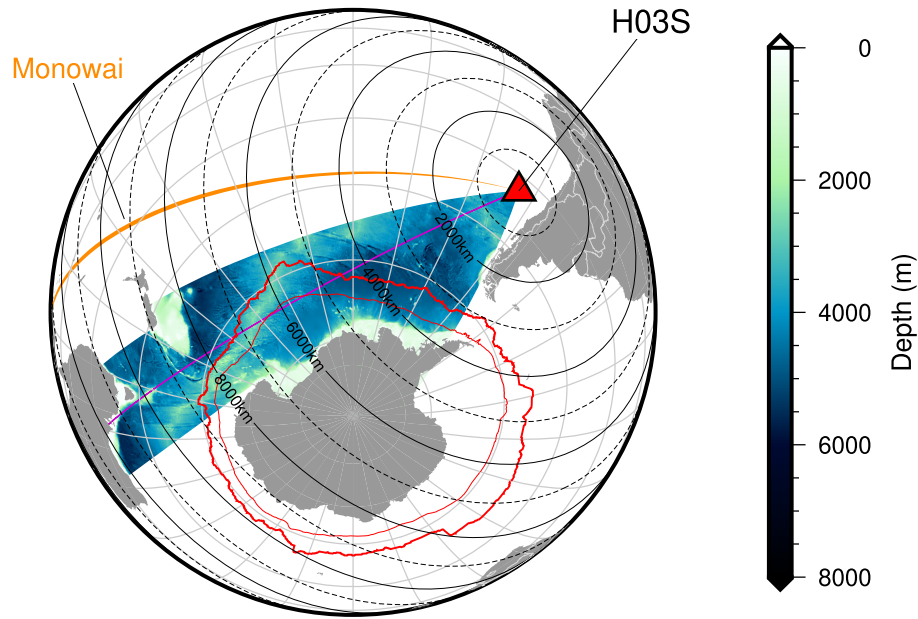$$\Delta t_{S1-S2} = \vec{p} \cdot r_2 - \vec{p} \cdot r_1$$

Figure 5. Map of the southern hemisphere indicate two main areas of activity of Fig. 4. H03S is marked by the red triangle. Back projections from H03S in the direction of 210° and 242° are given by the magenta and orange lines, respectively. The swath shows the bathymetry between 172° and 224° (General Bathymetric Chart of the Oceans, GEBCO, Weatherall *et al.* 2015). The red contour lines indicate the total (thick) and the average (thin) ERA5 sea ice extent for the entire period.
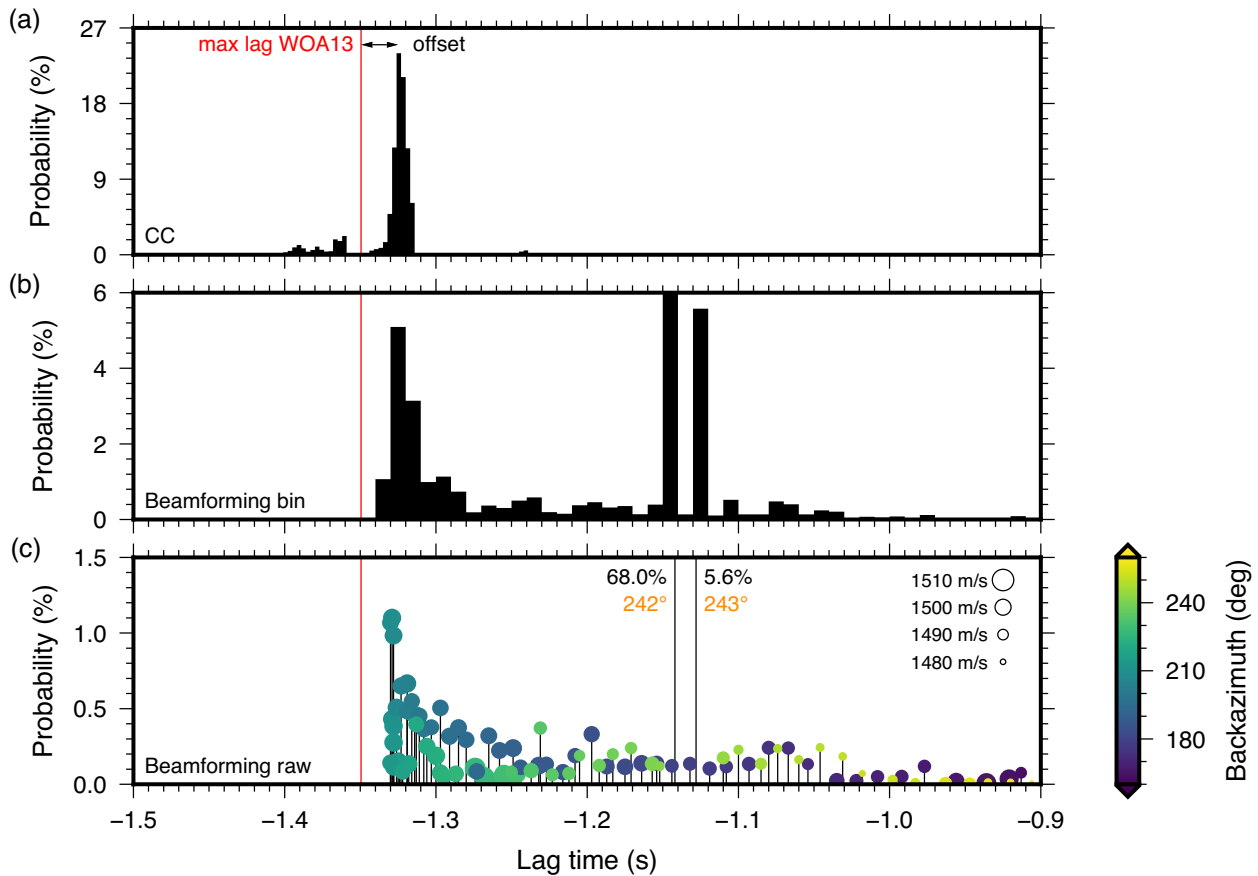

Figure 6. Lag time probability for H03 S1–S2 retrieved from (a) cross-correlations (CC) and (b–c) plane wave beamforming. Beamforming lag times are (b) binned per 10 ms and (c) raw estimates for the dominant slowness per backazimuth. The red vertical line indicates the approximated maximum lag time using the WOA13 annual climatological mean speed of sound for 2005–2012.

for every mean slowness per backazimuth as defined in Fig. 4(c), only considering apparent velocities with a confidence interval below 2 m s^{-1} (black squares). Probabilities in the raw lag estimates of Fig. 6(c) are obtained from Fig. 4(a). The reversing colour gradient at the maximum negative lag time and higher density of detections illustrate that a large fraction of the detections are located within the Fresnel zone of S1–S2. However, these detections are characterized by an increased apparent velocity. Two primary plane wave delay estimates are related to the Monowai volcano, at a backazimuth of 242° and 243° with apparent velocities of 1485 and 1487 m s^{-1}, yielding lag times of −1.145 and −1.128 s. Binned plane wave delay estimates indicate a similar slightly slower peak lag time as retrieved from cross-correlations.

The retrieved CC lag time for propagation along the receiver pair S1–S2 (−1.324 ±0.011 s) separated by 1999.6 m yields a local speed of sound $c = 1510.2$ ±13.0 m s^{-1}. Substituting into eq. (2) for a mean depth $z = 823.9$ m yields a temperature of 10.4 ± 2.8 °C. This is too large to be physically reasonable. The expected annual climatological mean temperature is 4.6 °C based on the World Ocean Atlas (WOA13; Locarnini *et al.* 2013) for 2005–2012 at a mean depth of 825 m (averaged between climatologies for 800 and 850 m depth). The corresponding climatological mean speed of sound, using eq. (1) and a salinity of 34.3 (WOA13; Zweng *et al.* 2012), is 1481.7 m s^{-1} yielding an expected lag time of −1.349 s, indicated by the red vertical line in Fig. 6. Retrieved peak lag times by both cross-correlations and array processing are significantly lower than the WOA13 lag time, discussed in Section 6.

5 SOURCE SPECTRAL CHARACTERIZATION

5.1 Spectrograms

Fig. 7 shows the hourly spectrogram at H03S1 applying the method of Welch (1967). In this method, spectrum levels for 4.1 s sub-windows (1024 samples) are stacked and averaged per hour. The frequency spectra show a clear seasonal trend, similar to results as obtained by Matsumoto *et al.* (2014) for the years 2002–2008 at H03N. Three different periods are distinguished:

(i) January–March (JFM) shows the highest average spectrum level combined with frequently occurring impulsive broadband signals. The broadband range and the pulse like behaviour during JFM is most likely related to iceberg break-up and disintegration processes, occurring predominantly during the austral summer and autumn (Dziak *et al.* 2013).

(ii) April–September (A–S) marked by a well-constrained peak within the 15–20 Hz frequency band. McDonald *et al.* (1995), Andrew *et al.* (2011) and Dziak *et al.* (2015) observed similar typical gliding harmonics usually associated with Baleen whale calls. These mammals, mostly Fin and Blue whales, can be recognized by their sound signature centred around 17 Hz. Whales can be largely present near Robinson Crusoe Island (Haralabus *et al.* 2014), especially during the Antarctic winter when they prefer to migrate to higher latitudes to breed and give birth. Therefore, we interpret the observed signature between 15 and 20 Hz during A–S to be whale noise.

(iii) October–December (OND) characterized by significantly less activity along the entire frequency spectrum of interest.

5.2 Comparison with Knudsen

Fig. 8 shows the averaged spectra of the three periods indicated in Fig. 7 for 2015 and 2016 compared to the so-called Knudsen spectral empirical noise levels (Wenz 1962). The Knudsen spectra are based on a large amount of noise measurements in deep water and describe the hydroacoustic ambient noise field for different frequency bandwidths. For low frequencies, less than 10 Hz, turbulence is typically the main source. Between 50 and 500 Hz distant shipping becomes important. Above this range (up to 25 kHz) the ambient noise level depends on the breaking of capillary surface waves, depending on the sea state, which is primary influenced by the wind speed and surface pressure (Krauss 1973).

The indicated periods in Fig. 8 follow a similar trend as the Knudsen curve for frequencies less than 2 Hz. Moreover, all three lines show the cut-off anti-alias filter at 100 Hz which is in agreement with the hydrophone settings (Haralabus *et al.* 2014). The frequency spectrum of JFM (blue) follows the same trend as the Knudsen curve, but shows a higher spectrum level for 3–20 Hz. Heavy shipping is not expected in the area around H03S. Hence, iceberg related noise is most likely missing in the Knudsen curve. The period A–S shows a clear increase in spectrum level in the range 15–25 Hz (likely whale noise). Outside this range, A–S behaves very similar to OND.

5.3 Seasonal iceberg noise variations

The RMS amplitude of the array best-beam for each detection within the swath of Fig. 5 is determined to study the seasonal mechanisms of the noise sources, in particular iceberg noise. Only signals with SNR ≥ 0.9 between 3 and 15 Hz are considered to exclude whale noise. Fig. 9 shows the monthly averaged daily mean sound pressure level (SPL) combined with the ERA5 reanalysis data set. The relation between sea ice cover and the observed SPL as been identified by Matsumoto *et al.* (2014) for at H03N in the Southern Hemisphere and by Roth *et al.* (2012) for the Arctic Ocean. Iceberg sound is created when these icebergs collide and/or disintegrate into the open ocean (Dziak *et al.* 2013). Here, the SPL is compared to the total sea ice cover and the average normalized stress into the ocean τ_{oc} within the swath between 172° and 224° of Fig. 5. Monthly averaged daily mean sea ice cover as well as the normalized stress into the ocean are provided intrinsically by the ERA5 reanalysis data set with a horizontal resolution of 31 km. τ_{oc} is the momentum flux from the surface wind into the ocean normalized by the product of the air density and the square of air side friction velocity. τ_{oc} peaks in summer due to strong surface winds during the storm season in the Southern Ocean and South Pacific Ocean. Wind wave activity in terms of significant–wave–height (SWH; Janssen 2004), however, reaches its maximum during the austral winter.

Maximum SPL is observed near the end of austral summer. Maximum SPL coincides with the minimum in sea ice cover (near the maximum sea ice cover growth) and the maximum normalized stress into the ocean. During this period, the concentration of drifting icebergs increases as well as the wave-wind activity. As such, both the number of events and corresponding SPL increases. According to the Knudsen curve (Fig. 8), the local ambient noise field is influenced by wind speed and severe weather conditions at much higher frequencies (500 Hz–25 kHz). However, it is suggested that τ_{oc} and so surface wind (and SWH) has an indirect influence on the detected sound level by (in)directly affecting the iceberg collision and disintegration processes.
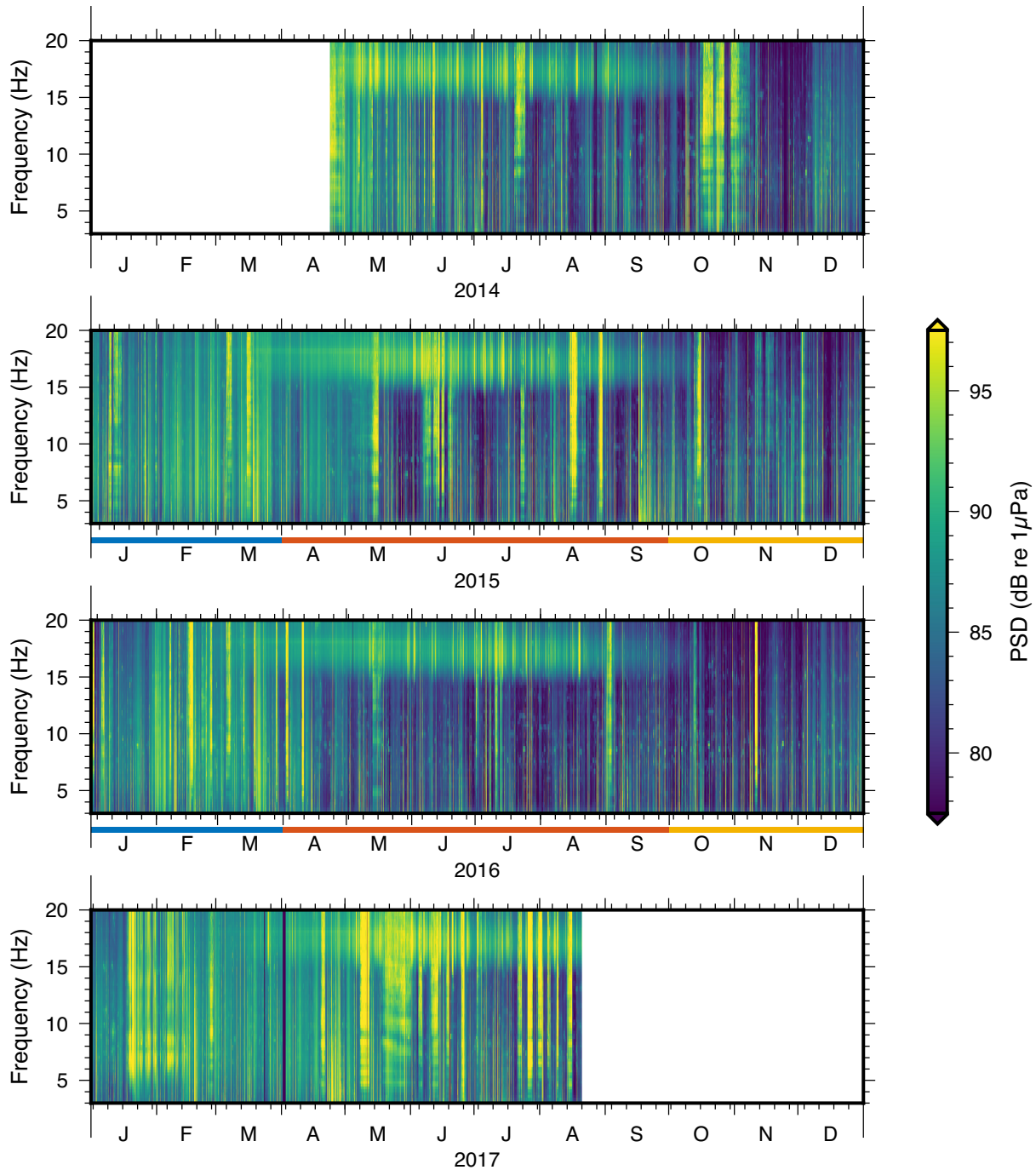
Figure 7. Power spectral density (PSD) per hour for H03S1 applying the method of Welch (1967) for 4.1s subwindows. No overlap is present between different hours. Hours containing gaps are removed. Three periods of interest are marked in 2015 and 2016: JFM (blue), A–S (red) and OND (orange).

6 DISCUSSION

Beamforming reveals a clear systematic directional trend in apparent velocity (Fig. 4c), suggesting azimuthally dependent mode propagation. In the farfield, lateral variability in bathymetry can lead to out-of-plane effects (Heaney *et al.* 2017), whereas lateral variations of the sound speed profile can induce directional variations in acoustic propagation modes (Munk *et al.* 1988; Heaney *et al.* 1991; de Groot-Hedlin *et al.* 2009). In the nearfield, speed of sound variations between the hydrophones can affect modal propagation. In addition, tilting of the array normal can play a significant role in

the observed apparent velocity (Edwards & Green 2012). Nonetheless, the 0.6° tilt for H03S yields a maximum apparent velocity error of only 4 m s⁻¹ for highly inclined signals along the angle of maximal plunge, which does not explain the observed trend. Fig. 1 indicates a significant slope in the bathymetry near H03S towards the south. Therefore, our hypothesis is that this slope directionally affects the shape of the local sound channel and so nearfield propagation. Hence, signals arrive at the array with a non-zero inclination angle with the result that the thermometry application does not work for H03S.
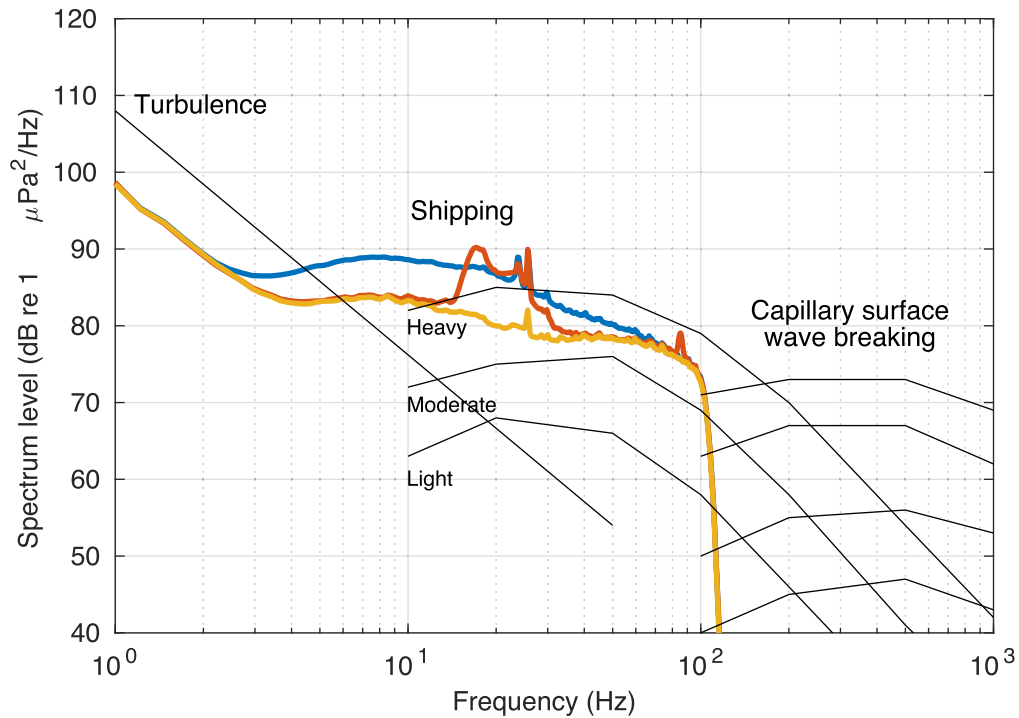
Figure 8. Averaged power spectral density of the periods JFM (blue), A–S (red) and OND (orange) for 2015 and 2016 (see Fig. 7) with theoretical Knudsen spectra (black).
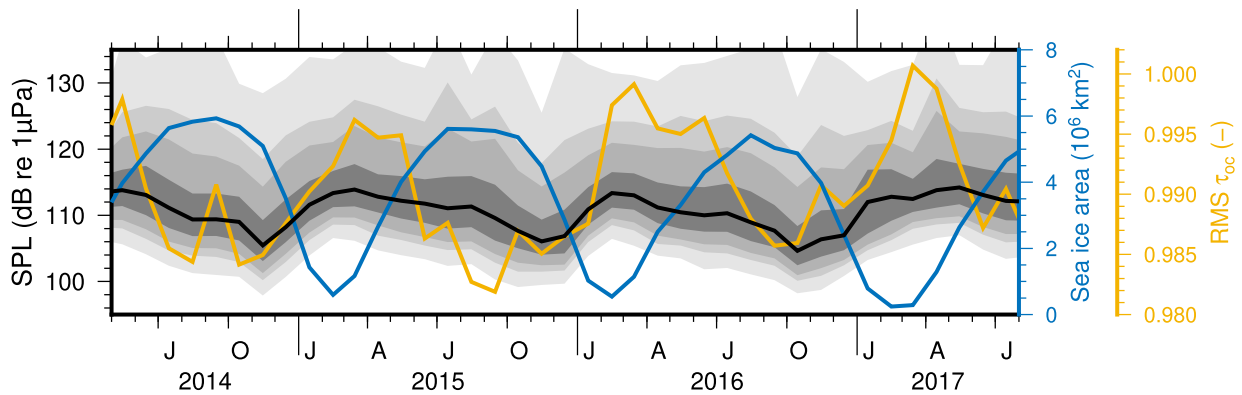
Figure 9. Monthly averaged daily mean sound pressure level (SPL) for the swath of Fig. 5. The grey shades represent the SPL quantile distribution for percentiles 1–99, 5–95, 10–90 and 25–75 per cent, from light to dark, respectively. The solid black line is the median SPL. The coloured lines are the ERA5 total sea ice area (blue) and the average normalized stress into the ocean (yellow) for the similar swath.

The impact is similar to a tilted array, yielding higher apparent velocities along the maximal plunge direction and a maximum backazimuth error in the minimal plunge direction. The directional variation in mean apparent velocity is in agreement with the slope. This hypothesis is supported by the apparent separation associated with an inclined plane wave, under the assumption that the separation of the sensors is correct and the signals propagate with the climatological speed of sound of 1481.7 m s^{-1}. The apparent separation for S1–S2 according to cross-correlations yields 1952.9 m corresponding to an incidence angle of 12.4° from the horizontal. Similarly, the apparent velocity of 1502 m s^{-1} in the direction of 210° obtained by beamforming yields an inclined plane wave with an angle of 9.4° according to eq. (5). For comparison, the maximum and average slope underneath H03S, based on the General Bathymetric Chart of the Oceans (GEBCO; Weatherall *et al.* 2015), equals −13 and −8 per cent, respectively, with a heading of 207°.

However, the direct relation between the bathymetric slope and its spatial extent and the incidence angle of the signals is unclear. Metz *et al.* (2018) indicated a systematic counterclockwise deviation of 0.4° for the observed signal of the Monowai Seamount compared to the true geodesic angle of arrival. This deviation could partially be attributed to the indirect effect of the steep slope near H03S as indicated by array processing and cross-correlations. In this study, the obtained deviation is larger; however, this can partly be associated with the coarser slowness grid used for beamforming. Increasing the slowness grid to smaller steps while supporting subsample time-shifts by, for example, oversampling using interpolation, increases the array processing accuracy.

It is recommended to verify these bathymetric effects by propagation modelling, using high-resolution bathymetry and velocity models, and analysing all IMS hydroacoustic arrays. In addition, the observed blocking by Robinson Crusoe Island's topographic spur

is more or less aligned with the steepest slope near H03S (see solid black line in Fig. 1). This implies that the steep slope narrows the array field of view.

The concept of thermometry by cross-correlations of closely spaced receivers demonstrates the sensitivity of the method. Small variations in estimated lag time will have a significant impact on the retrieved velocity and so the estimated temperature. For a receiver pair distance of only 2 km, temporal resolution in the order of milliseconds is essential. Hence, spatial variation of the sensor locations over time due to the streaming of the water can already be problematic (Nichols & Bradley 2017). In this study, it is assumed that sources of S1–S2 are located within the Fresnel zone which should correspond to maximum lag time propagation. The latter is based on along pair propagation, notwithstanding, clear evidence of increased apparent velocity is revealed by array processing as indicated in Fig.   4(c). The latter suggests vertically inclined waves, significantly shortening the relative distance between S1 and S2. Hence, maximum lag time propagation is no longer valid. Cross-correlations of S2–S3 and S3–S1 demonstrate that the ambient noise field is not sufficiently equipartitioned. A non-isotropic noise field significantly affects the lag time (Weaver *et al.* 2009). This lag time error can be estimated from a particular non-isotropic distribution of recorded wave intensity (Froment *et al.* 2010). Recent studies by Woolfe *et al.* (2015) and Evers *et al.* (2017) are probably affected by similar uncertainties, however, the relative errors are much smaller due to the much longer lengthscale, with intersensor distances greater than 100 km. The concept of thermometry, even for such small receiver distances, can be improved by retrieving stationary lag times of multiple sources (Snieder *et al.* 2007). Variations of the ambient noise field can significantly affect the pair-wise cross-correlation results. Therefore, it is suggested to combine cross-correlations and array processing techniques for multiple frequency bands to optimally benefit from various source characteristics.

7 CONCLUSION

The ambient noise field at H03S between 2014 April 23 and 2017 August 20 is characterized by cross-correlations, array processing and spectral analysis. Multiple mechanisms affect the acoustic ambient noise field. It is demonstrated that the pre-processing of the cross-correlation data applying one-bit normalization successfully suppresses undesired transient events such as earthquakes. Stacked cross-correlations do not yield a coherent array signal. Stacked envelopes of the cross-correlations, however, indicate a coherent signal approaching H03S from a south–southwest direction. Array processing by plane wave beamforming identifies two main source directions: Antarctica (172°–224°) and the Monowai Seamount (242°). Hence, the retrieved cross-correlation lag time of S1–S2 corresponds to the Antarctic coast whereas receiver pairs S2–S3 and S3–S1 are most likely related to the Monowai Seamount. Spectral analysis supports that the observed ambient noise field exists of iceberg noise from Antarctica, volcanic signal from Monowai, as well as baleen whales around the array (15–20 Hz). The results agree with the expected noise levels according to the Knudsen curve. The best-beam SPL indicates a clear seasonal variation that is associated with ERA5 climatological data on sea ice cover and normalized stress into the ocean. Maximum SPL is received during minimal sea ice cover and peak normalized stress at the end of austral summer. During this storm season, both ice growth and surface

winds are maximum. The actual mechanism behind this remained unclear during this study, but could be of interest for future work.

Acoustic thermometry on a single IMS station is demonstrated for the hydrophones H03 S1–S2 using continuous source field dominated by iceberg noise from Antarctica. Nonetheless, classical interferometry assuming a homogeneous medium is not valid. Cross-correlation and array processing indicate significant directional variation in local propagation observed as inclined signals from the horizontal, most likely related to the steep slope in the bathymetry near H03S. It is recommended to further investigate this effect due to its potential impact on the verification of the CTBT. In addition, it is demonstrated that the ambient noise field is not sufficiently equipartitioned, in particular for thermometry applied to a single IMS station. It is shown that this causes a large error in the estimated temperature, primarily due to the short receiver spacing. These large errors have not been addressed in previous studies on deep-ocean acoustic thermometry.

REFERENCES

Andrew, R.K., Howe, B.M. & Mercer, J.A., 2011. Long-time trends in ship traffic noise for four sites off the North American West Coast, *J. acoust. Soc. Am.,* **129**(2), 642–651.

Bakulin, A. & Calvert, R., 2006. The virtual source method: theory and case study, *Geophysics,* **71**(4), SI139–SI150.

Bensen, G.D., Ritzwoller, M.H., Barmin, M.P., Levshin, A.L., Lin, F., Moschetti, M.P., Shapiro, N.M. & Yang, Y., 2007. Processing seismic ambient noise data to obtain reliable broad-band surface wave dispersion measurements, *Geophys. J. Int.,* **169**(3), 1239–1260.

Boschi, L. & Weemstra, C., 2015. Stationary-phase integrals in the cross correlation of ambient noise, *Rev. Geophys.,* **53**(2), 411–451.

Boschi, L., Weemstra, C., Verbeke, J., Ekström, G., Zunino, A. & Giardini, D., 2013. On measuring surface wave phase velocity from station-station cross-correlation of ambient signal, *Geophys. J. Int.,* **192**(1), 346–358.

Chapp, E., Bohnenstiehl, D.R. & Tolstoy, M., 2005. Sound-channel observations of ice-generated tremor in the Indian Ocean, *Geochem. Geophys. Geosyst.,* **6**(6), doi:10.1029/2004GC000889.

Dahlman, O., Mykkeltveit, S. & Haak, H., 2009. Monitoring technologies, in *Nuclear Test Ban,* Chap. 2, pp. 25–58, Springer, Netherlands, Dordrecht.

de Groot-Hedlin, C., Blackman, D.K. & Jenkins, C.S., 2009. Effects of variability associated with the Antarctic circumpolar current on sound propagation in the ocean, *Geophys. J. Int.,* **176**(2), 478–490.

de Groot-Hedlin, C.D., 2005. Estimation of the rupture length and velocity of the Great Sumatra earthquake of Dec 26, 2004 using hydroacoustic signals, *Geophys. Res. Lett.,* **32**(11), 1–4.

Dushaw, B.D. *et al.*, 2009. A decade of acoustic thermometry in the North Pacific Ocean, *J. geophys. Res.,* **114**(7), C07021, doi:10.1029/2008JC005124.

Dziak, R., Fowler, M., Matsumoto, H., Bohnenstiehl, D., Park, M., Warren, K. & Lee, W.S., 2013. Life and death sounds of iceberg A53a, *Oceanography,* **26**(2), doi:10.5670/oceanog.2013.20.

Dziak, R.P. *et al.*, 2015. Sources and levels of ambient ocean sound near the Antarctic Peninsula, *PLoS One,* **10**(4), e0123425, doi:10.1371/journal.pone.0123425.

Edwards, W.N. & Green, D.N., 2012. Effect of interarray elevation differences on infrasound beamforming, *Geophys. J. Int.,* **190**(1), 335–346.

Evers, L.G. & Snellen, M., 2015. Passive probing of the sound fixing and ranging channel with hydro-acoustic observations from ridge earthquakes, *J. acoust. Soc. Am.,* **137**(4), 2124–2136.

Evers, L.G., Green, D.N., Young, N.W. & Snellen, M., 2013. Remote hydroacoustic sensing of large icebergs in the southern Indian Ocean: implications for iceberg monitoring, *Geophys. Res. Lett.,* **40**(17), 4694–4699.

Evers, L.G., Wapenaar, K., Heaney, K.D. & Snellen, M., 2017. Deep ocean sound speed characteristics passively derived from the ambient acoustic noise field, *Geophys. J. Int.,* **210**(1), 27–33.

Froment, B., Campillo, M., Roux, P., Gouédard, P., Verdel, A. & Weaver, R.L., 2010. Estimation of the effect of nonisotropically distributed energy on the apparent arrival time in correlations, *Geophysics,* **75**(5), SA85–SA93.

Green, D.N., Evers, L.G., Fee, D., Matoza, R.S., Snellen, M., Smets, P. & Simons, D., 2013. Hydroacoustic, infrasonic and seismic monitoring of the submarine eruptive activity and sub-aerial plume generation at South Sarigan, May 2010, *J. Volc. Geotherm. Res.,* **257**, 31–43.

Haralabus, G., Pautet, L., Stanley, J. & Zampolli, M., 2014. Welcome back HA03 Robinson Crusoe Island, *CTBTO Spectr.,* **22**, 18–22.

Heaney, K.D., Kuperman, W.A. & McDonald, B.E., 1991. Perth-Bermuda sound propagation (1960): adiabatic mode interpretation, *J. acoust. Soc. Am.,* **90**(5), 2586–2594.

Heaney, K.D., Prior, M. & Campbell, R.L., 2017. Bathymetric diffraction of basin-scale hydroacoustic signals, *J. acoust. Soc. Am.,* **141**(2), 878–885.

Hersbach, H. & Dick, L., 2016. ERA5 reanalysis is in production, *ECMWF Newsl.,* **147**, 7.

Janssen, P., 2004. *On the Generation of Ocean Waves by Wind,* pp. 56–128, Cambridge Univ. Press, Cambridge.

Jensen, F.B., Kuperman, W.A., Porter, M.B. & Schmidt, H., 2011. *Computational Ocean Acoustics,* 2nd edn, Springer.

Krauss, W., 1973. *Dynamics of the Homogeneous and Quasihomogeneous Ocean,* Borntraeger.

Locarnini, R.A. *et al.*, 2013. World Ocean Atlas 2013 Volume 1: Temperature, Tech. Rep., National Oceanic and Atmospheric Administration.

Matsumoto, H., Bohnenstiehl, D.R., Tournadre, J., Dziak, R.P., Haxel, J.H., Lau, T.-K.A., Fowler, M. & Salo, S.A., 2014. Antarctic icebergs: a significant natural ocean sound source in the Southern Hemisphere, *Geochem. Geophys. Geosyst.,* **15**(8), 3448–3458.

McDonald, M.A., Hildebrand, J.A. & Webb, S.C., 1995. Blue and fin whales observed on a seafloor array in the Northeast Pacific, *J. acoust. Soc. Am.,* **98**(2), 712–721.

Medwin, H. & Clay, C.S.C.S., 1997. *Fundamentals of Acoustical Oceanography,* Academic Press.

Melton, B.S. & Bailey, L.F., 1957. Multiple signal correlators, *Geophysics,* **22**(3), 565–588.

Metz, D., Watts, A.B., Grevemeyer, I., Rodgers, M. & Paulatto, M., 2016. Ultra-long-range hydroacoustic observations of submarine volcanic activity at Monowai, Kermadec Arc, *Geophys. Res. Lett.,* **43**(4), 1529–1536.

Metz, D., Watts, A.B., Grevemeyer, I. & Rodgers, M., 2018. Tracking submarine volcanic activity at Monowai: constraints from long-range hydroacoustic measurements, *J. geophys. Res.,* **123**(9), 7877–7895.

Munk, W.H., O'Reilly, W.C., Reid, J.L., Munk, W.H., O'Reilly, W.C. & Reid, J.L., 1988. Australia-Bermuda sound transmission experiment (1960) revisited, *J. Phys. Oceanogr.,* **18**(12), 1876–1898.

Nichols, S.M. & Bradley, D.L., 2017. *In situ* shape estimation of triangular moored hydrophone arrays using ambient signals, *IEEE J. Ocean. Eng.,* **42**(4), 923–935.

Prior, M., Brown, D., Haralabus, G. & Stanley, J., Institute of Acoustics (Great Britain), 2012. Long-term monitoring of ambient noise at CTBTO hydrophone stations, in *Proceedings of the 11th European Conference on Underwater Acoustics,* pp. 1018–1025, Institute of Acoustics, St. Albans.

Roth, E.H., Hildebrand, J.A., Wiggins, S.M. & Ross, D., 2012. Underwater ambient noise on the Chukchi Sea continental slope from 2006-2009, *J. acoust. Soc. Am.,* **131**(1), 104–110.

Roux, P. & Kuperman, W.A., 2004. Extracting coherent wave fronts from acoustic ambient noise in the ocean, *J. acoust. Soc. Am.,* **116**(4), 1995–2003.

Shapiro, N.M. & Campillo, M., 2004. Emergence of broadband Rayleigh waves from correlations of the ambient seismic noise, *Geophys. Res. Lett.,* **31**(7), L07614, doi:10.1029/2004GL019491.

Snieder, R., 2004. Extracting the Green's function from the correlation of coda waves: a derivation based on stationary phase, *Phys. Rev. E,* **69**(4), 8.

Snieder, R., Wapenaar, K. & Wegler, U., 2007. Unified Green's function retrieval by cross-correlation; connection with energy principles, *Phys. Rev. E,* **75**(3), 036103.

Talandier, J., Hyvernaud, O., Okal, E.A. & Piserchia, P.F., 2002. Long-range detection of hydroacoustic signals from large icebergs in the Ross Sea, Antarctica, *Earth planet. Sci. Lett.,* **203**(1), 519–534.

Talandier, J., Hyvernaud, O., Reymond, D. & Okal, E.A., 2006. Hydroacoustic signals generated by parked and drifting icebergs in the Southern Indian and Pacific Oceans, *Geophys. J. Int.,* **165**(3), 817–834.

Wapenaar, K., Fokkema, J. & Snieder, R., 2005. Retrieving the Green's function in an open system by cross correlation: a comparison of approaches (L), *J. acoust. Soc. Am.,* **118**(5), 2783–2786.

Wapenaar, K., Draganov, D., Snieder, R., Campman, X. & Verdel, A., 2010. Tutorial on seismic interferometry: part 1 - basic principles and applications, *Geophysics,* **75**(5), 75A195–75A209.

Watts, A.B. *et al.*, 2012. Rapid rates of growth and collapse of Monowai submarine volcano in the Kermadec Arc, *Nature Geosci.,* **5**, 510–515.

Weatherall, P. *et al.*, 2015. A new digital bathymetric model of the world's oceans, *Earth Space Sci.,* **2**, 1–15.

Weaver, R., Froment, B. & Campillo, M., 2009. On the correlation of nonisotropically distributed ballistic scalar diffuse waves, *J. acoust. Soc. Am.,* **126**(4), 1817.

Welch, P., 1967. The use of fast Fourier transform for the estimation of power spectra: a method based on time averaging over short, modified periodograms, *IEEE Trans. Audio Electroacoust.,* **15**(2), 70–73.

Wenz, G.M., 1962. Acoustic ambient noise in the ocean: spectra and sources, *J. acoust. Soc. Am.,* **34**(12), 1936–1956.

Wessel, P., Smith, W.H., Scharroo, R., Luis, J. & Wobbe, F., 2013. Generic mapping tools: improved version released, *EOS, Trans. Am. geophys. Un.,* **94**(45), 409–410.

Woolfe, K.F., Lani, S., Sabra, K.G. & Kuperman, W.A., 2015. Monitoring deep-ocean temperatures using acoustic ambient noise, *Geophys. Res. Lett.,* **42**(8), 2878–2884.

Zweng, M.M. *et al.*, 2012. World Ocean Atlas 2013, Volume 2: Salinity, Tech. Rep., National Oceanic and Atmospheric Administration.